Quantum dot in a well infrared photodetectors for high operating temperature focal plane arrays

S.Tsao, T. Yamanaka, S. Abdollahi Pour, I-K Park, B. Movaghar, and M. Razeghi[a]
Center for Quantum Devices,[b] Department of Electrical Engineering and Computer Science, Northwestern University, Evanston, Illinois 60208

ABSTRACT

InAs quantum dots embedded in InGaAs quantum wells with InAlAs barriers on InP substrate grown by metalorganic chemical vapor deposition are utilized for high operating temperature detectors and focal plane arrays in the middle wavelength infrared. This dot-well combination is unique because the small band offset between the InAs dots and the InGaAs well leads to weak dot confinement of carriers. As a result, the device behavior differs significantly from that in the more common dot systems that have stronger confinement. Here, we present energy level modeling of our QD-QW system and apply these results to interpret the detector behavior. Detectors showed high performance with D* over 10^{10} cmHz$^{1/2}$/W at 150 K operating temperature and with high quantum efficiency over 50%. Focal plane arrays have been demonstrated operating at high temperature due to the low dark current observed in these devices.

Keywords: quantum dot, infrared, photodetector, InP, focal plane array, MOCVD

1. INTRODUCTION

Self-assembled semiconductor quantum dots (QDs)[1] have attracted a great deal of attention because of their novel properties and possible applications such as quantum dot infrared photodetectors (QDIPs)[2,3,4,5]. QD-based detectors can be building blocks of focal plane arrays (FPAs) in infrared imaging systems which have been widely investigated for mid-infrared (3~5 μm) and long-infrared (8~12 μm) applications[6,7,8]. QD-based inrafred detector have been subject to intensive research because they are expected to outperform current quantum well infrared photodetectors (QWIPs)[9,10,] due to their i) intrinsic sensitivity to normal incidence light, ii) longer life time of the photo-excited electrons due to the reduced recombination rate associated with a multi-phonon relaxation step, and iii) lower dark and noise currents.[11] In particular, the lower dark currents enable higher operating temperatures. Achieving higher operating temperatures will reduce the cost and complexity of detector and imaging systems by reducing the cooling requirements normally associated with detector systems running at cryogenic temperature. Pure QD-based detectors structures have been extensively studied with many showing promise for high performance [5,12,3,] however, recent work seems to have shifted more to QD-QW combination devices[7,13,14,15] such as the dot-in-a-well (DWELL) structure. Here, we present recent theoretical and experimental developments on our own QD-QW hybrid structure detectors that show high detectivity and quantum efficiency at high operating temperatures. This detector structure was also applied to a 320 × 256 focal plane array with high operating temperature capability.

2. QDWIP THEORY AND MODELING

Our QDWIP detector technology different from many conventional DWELL detectors in the following two ways: 1) in our structures the QDs are not placed in the center of the QW and more significantly, 2) our dot-well material combination results in a very shallow dot potential relative to the well. This can have significant implications on the device performance. To better understand the effects of this shallow potential, we have developed a theoretical model of the quantum dot/quantum well hybrid system's energy levels. This section presents this theoretical modeling of the QDWIP.

[a] Electronic mail: razeghi@eecs.northwestern.edu
[b] Internet: http://cqd.ece.northwestern.edu

Quantum Dots, Particles, and Nanoclusters VI,
edited by Kurt G. Eyink, Frank Szmulowicz, Diana L. Huffaker, Proc. of SPIE Vol. 7224,
72240V · © 2009 SPIE · CCC code: 0277-786X/09/$18 · doi: 10.1117/12.809251

The QDWIP device structure is shown in Fig. 1 along with a band diagram schematic of the energy levels. The structure utilizes as the absorbing element InAs QDs grown on an InAlAs barrier and capped with an InGaAs QW followed by an InAlAs barrier. The InAlAs and InGaAs are lattice matched to the InP substrate. In this section we develop a model to obtain the detailed energy level structure that is depicted in the band diagram picture of Fig. 1.

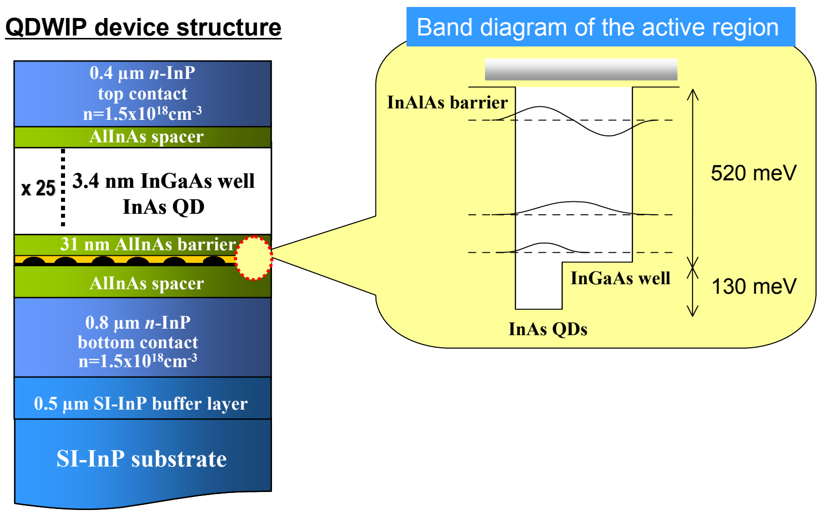

Fig. 1 Device structure schematic

Even though there are some efforts to investigate the energy states in QDs,[16,17] it is generally hard to analytically calculate the energy levels for arbitrary 3D geometries. In the present work, we used COMSOL Multiphysics®, a finite element method software package, to calculate the energy levels in our QDWIP structure. Fig. 2(a) shows the schematic picture of the geometry for the calculation. The QD is set in a box 64 nm × 64 nm × 40 nm, and periodic boundary conditions are applied. Fig. 2(b) shows the cross-section around the QD. The geometries are based on representative experimental results of the QD density, size, and shape. It is noted that the wetting layer (WL) thickness is uncertain and was treated as a fitting parameter.

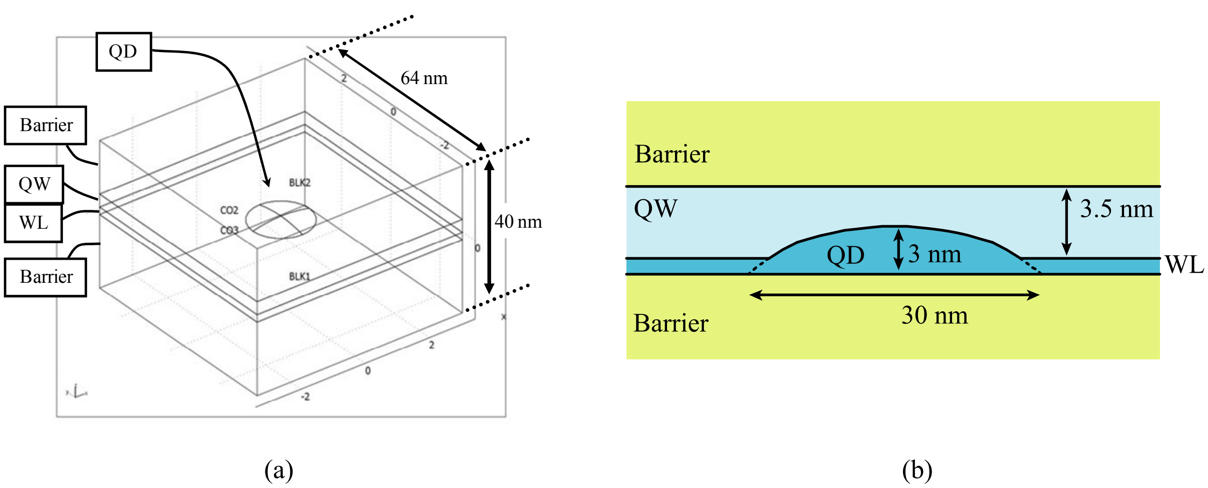

Fig. 2. The left image (a) is a schematic picture of the geometry for the energy level calculation and the right (b) is a cross-sectional drawing around the QD.

In Fig. 3, the distributions of the obtained wavefunctions are plotted for the plane through in the middle of the WL. The first state was found to be clearly bound to the QD as shown in Fig. 3(a). However, in the second and third states, the wavefunctions seem to be delocalized as shown in Fig. 3(b) and (c), and thus these states are considered to be unbound states, or in other words, QW-like states. In actuality, the model found many states above these states among which the energy separation is small, just like energy states with many *k*-values in the QW plane. The calculation showed that there is only one bound state in the conduction band in our QDWIP. If the QD-binding energy is evaluated by the energy difference between the QD-bound state and the first QW-like state, the QD-binding energy is about 30 meV as summarized in Table 1.

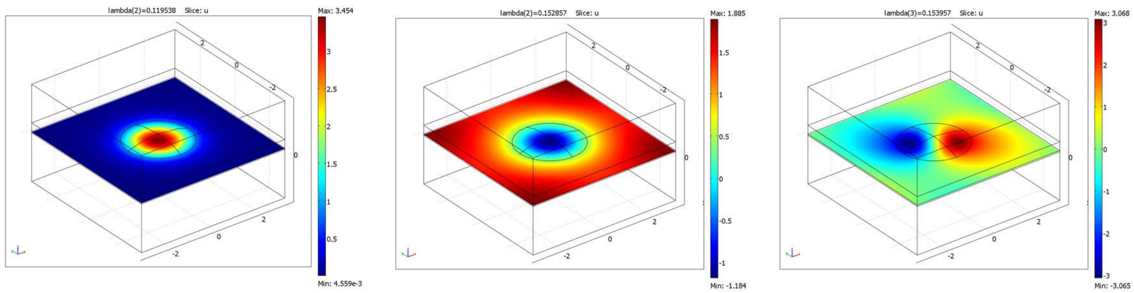

(a) (b) (c)

Fig. 3. The distribution of the calculated wavefunction for the first three eigenstates in the QDWIP for the WL thickness 0.6 nm.

Table 1 – QD binding energy for the different WL thicknesses

WL thickness	QD binding energy
0.6 nm	33.3 meV
0.8 nm	28.3 meV
1.0 nm	23.4 meV

To obtain the WL thickness in our QDWIP, experimentally obtained photo-luminescence (PL) results were compared to the calculation results. At room temperature, the QDWIPs typically showed a PL peak around 1350 nm (0.921 eV). Here, two cases are considered; one is the interband transition between the QD-bound states, and the other is the interband transition between the QW-like states. The calculation was then performed with different WL thicknesses, Table 2 shows the calculated energy difference between the QD-bound state in the conduction band and the first QD-bound state in the valence band, and Table 3 shows the calculated energy difference between the first QW-like state in the conduction band and the first QW-like state in the valence band. In the case of the QD bound states between the conduction and valence bands, the calculated transition energy is significantly smaller than the experimentally measured PL results. On the other hand, the calculated transition energy for the QW-like states between the conduction and valence bands becomes consistent with the experimental results for a WL thickness of 0.6 nm. Because the QD density is not high ~10^{10} /cm^2 and electrons can be easily excited from the QD-bound state to the QW-like state at room temperature, it is reasonable that the PL process is dominated by the transition between the QW-like states instead of the QD-bound states. Thus, the WL thickness in our QDWIP is considered to be 0.6 nm.

Table 2 – Calculated interband transition energy in the QD-bound states in QDWIPs

WL thickness	Transition energy (eV)	Corresponding wavelength
0.6 nm	0.733	1696 nm
0.8 nm	0.727	1711 nm
1.0 nm	0.721	1725 nm

Table 3 – Calculated interband transition energy in the QW-like states in QDWIPs

WL thickness	Transition energy (eV)	Corresponding wavelength
0.6 nm	0.903	1376 nm
0.8 nm	0.871	1428 nm
1.0 nm	0.840	1481 nm

Next, the intersubband transitions are discussed. To evaluate the energy level of the excited state, the energy dependence of the effective mass must be considered. Kane's formula is widely known as an expression of energy dependence of the effective mass including the non-parabolic effect,[18] and it is expected that the effective mass will increase when the electron energy increases as described by Eq.1,

$$m^*(E) = m_0^* \frac{E_g + E}{E_g} \qquad (1)$$

where m^*_0 is the effective mass at the bottom of the conduction band and E_g is the bandgap. However, it is unclear whether Kane's model, which is based on periodic crystals, can be applied to our QD-QW structures. As a consequence, the effective mass is treated as a fitting parameter and is multiplied by an arbitrary constant. The photocurrent spectra peaks are observed around 3.8–3.9 μm as shown in Fig. 6(a)

. Again, because the QD density is not high, the dominant process is expected to be the transition from the QW-like ground state to the QW-like excited state. The calculated energy separation between the ground state and the excited state in the QW-like states is summarized in Table 4. The calculated transition energy is consistent with the experimental result when $m^* = 1.5m^*_0$. In this case, the calculated excited state is found 0.474 eV above the bottom of the QW and the bandgap of $Ga_{0.47}In_{0.53}As$ is 0.752 eV, therefore the factor of 1.5 is close to the estimation by Kane's formula $m^* = 1.63m^*_0$ and is considered to be in adequate range. Finally, the obtained energy level structure is depicted in Fig. 4. This result will be utilized to develop our models of device level characteristics such as the photocurrent spectrum, which will be discussed later.

Table 4 – Calculated intersubband transition energy in QDWIPs (WL thickness 6 nm).

m^*/m^*_0	**Transition energy (eV)**	**Corresponding wavelength**
1.25	0.349	3.56 μm
1.50	0.321	3.87 μm
1.75	0.296	4.20 μm

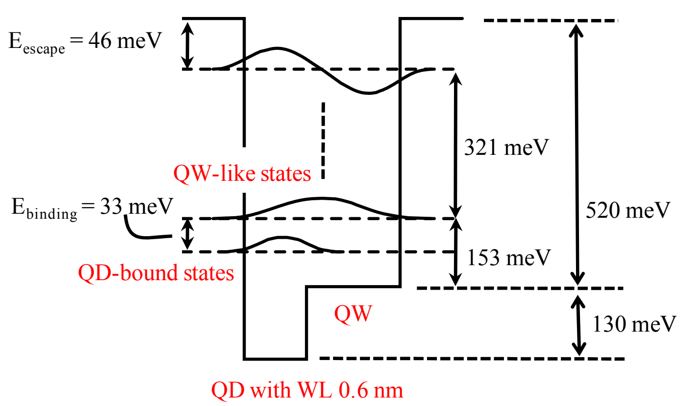

Fig. 4. Calculated energy level structure in QDWIPs

3. MATERIAL GROWTH

The device structure of Fig. 1 was grown by low-pressure metalorganic chemical vapor deposition (LP-MOCVD) in an Emcore Discovery reactor. Trimethylindium, triethylgallium, and trimethyaluminuim were used as group III precursors while pure phosphine, pure arsine and 5% dilute arsine were used as group V precursors. The growth temperature of the whole device structure was 570 °C. First, a 0.5 µm-thick undoped InP buffer layer followed by a 0.8 µm-thick bottom InP contact layer n-type doped to $n=1.5\times10^{18}cm^{-3}$ was grown. Then the active region was grown, consisting of 25 stacks of InAs QD/GaInAs QW layers with 31 nm-AlInAs barrier layers. The 3.5 nm-GaInAs QW layer on top of each QD layer had a doping level of $n=1\times10^{18}cm^{-3}$. Finally, we grew a 0.4 µm-thick top InP contact layer doped to $n=1.5\times10^{18}cm^{-3}$. The InAs QDs on the AlInAs barrier layers were obtained by self-assembly based on the Stranski-Krastanow epitaxial growth mode. The entire structure was grown on semi-insulating InP substrate. The InAlAs barriers are actually grown slightly lattice mismatched to compensate for the strain introduced into the structure by the QD layers.

Atomic force microscopy (AFM) images of the quantum dots in our device are shown in Fig. 5. The dot density is $\sim1\times10^{9}$ cm^{-2}. From AFM imaging experiments, the dots are approximately 6nm in height and 60 nm in diameter, though these sizes may be overestimated due to tip effects. These dots are larger than those in our previous reported devices.[19]

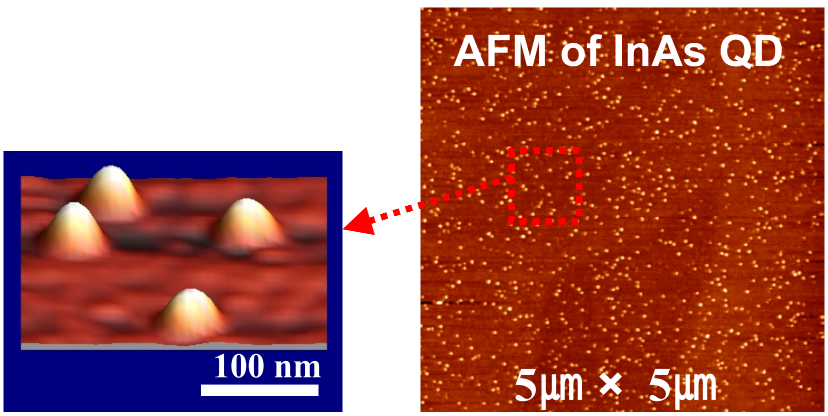

Fig. 5. Atomic force microscopy imaging of the InAs QDs used in our recent devices.

4. DEVICE FABRICATION AND TESTING

An array of 400×400 μm^2 detector mesas was fabricated in order to test the performance of the devices. The mesas were defined using conventional ultraviolet photolithography and dry etching by electron cyclotron resonance reactive ion etching. The Ti/Pt/Au top and bottom metal contacts were patterned via lift-off lithography, deposited via electron beam evaporation, and alloyed at 400ºC for 2 minutes. The sample was then mounted to a copper heatsink and attached to the cold finger of a liquid nitrogen cryostat equipped with a temperature controller for testing. The detection spectrum, responsivity, dark current, and noise current were measured. The optical measurements are taken in a normal incidence configuration. The dark current and noise current were measured by completely covering the detector with a copper "dark shield". The measurements were carried out as a function of bias and temperature.

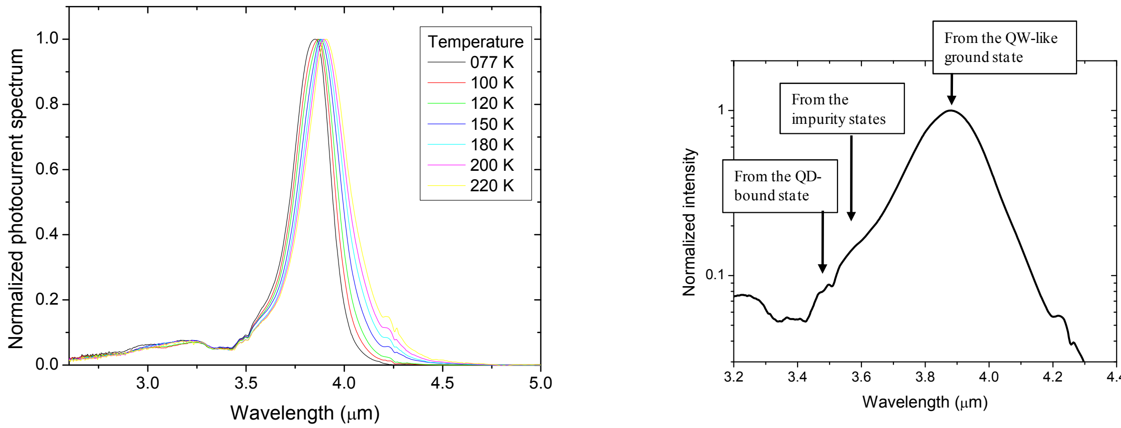

(a) (b)

Fig. 6. (a) Photocurrent spectrum of our QDWIPs as a function of temperature at fixed bias of –2V and (b) log scale plot of the photocurrent spectrum with the origin of the various shoulders/subpeaks are indicated.

The photocurrent spectrum was measured as a function of temperature and bias using a Mattson Galaxy 3000 Fourier transform infrared spectrometer. The spectral shape did not change significantly with bias or temperature as shown in Fig. 6(a). There is a consistent redshift and peak broadening with temperature. The peak detection wavelength is around 3.9μm. Also notable is the fact that the spectrum remains very clear even at temperatures as high as 220K. Now, we can compare the experimentally obtained photocurrent spectrum to the previously calculated energy level structure to gain some insight into the origin of the different shoulders and subpeaks present in Fig. 6(b), which shows a representative photocurrent spectrum in the QDWIP. The spectrum is plotted on a log scale to better emphasize the variations in the spectral shape. The main peak at 3.87 μm is very consistent with the calculated transition energy from the QW-like ground state to the QW-like excited state, 321 meV (3.87 μm). The calculation result shows the QD-bound state is 33 meV below the QW-like ground state. In this case, the transition energy from the QD-bound state to the QW-like excited state is 354 meV (3.51 μm) and the subpeak at 3.5 μm is actually observed in the experiments. In the experimentally obtained spectrum, there was another subpeak observed at a wavelength in between these two transitions. This subpeak is possibly caused by the transition from the dopant impurity state to the excited state because the dopant level can be expected to be roughly 20 meV below the ground state. Finally, a broad subpeak around 3.2-3.3 μm was observed and has been attributed to the ground-to-continuum transition.[20] This transition has not been theoretically evaluated yet.

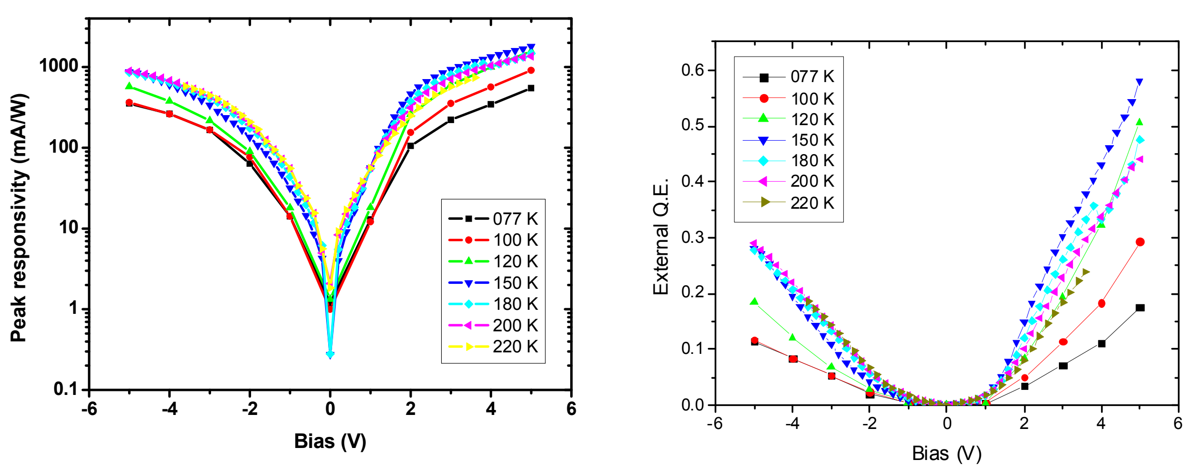

(a) (b)

Fig. 7. (a) Peak responsivity and (b) external quantum efficiency of our QDWIP device as function of temperature and bias.

The peak responsivity, however, has both a strong bias and temperature dependence as shown in Fig. 7(a). The absolute responsivity was measured using a calibrated blackbody source at 800°C and a lock-in amplifier. The highest value attained for the peak responsivity was 1.8 A/W at 150 K and 5V. This corresponds to an external quantum efficiency (QE) of 58% as shown in Fig. 7(b). The signal strength as a function of bias is significantly improved over our previous demonstration using this class of device as a result of improved material and dot optimization.[20] Of particular note, is the increased responsivity at lower temperatures and low biases, which is beneficial for our FPA applications. The external quantum efficiency data is shown on a linear scale to show the variation in response at the higher response ranges more clearly than can be seen in the peak responsivity plot of Fig. 7(a). Here we can see a strong asymmetry with bias where the positive bias side has a two times higher external QE. Above 150K the response starts to decrease with increased temperature. This is due to increased photocarrier recombination at high temperatures, as discussed our previous works.[20]

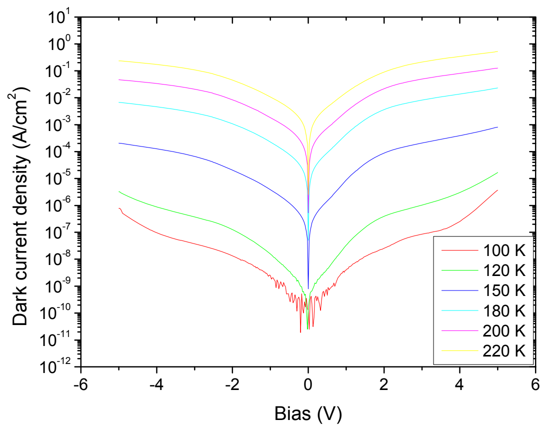

Fig. 8. Dark current density as a function of bias and temperature in our QDWIP.

The dark current density of the detector was measured with an Agilent 4156C semiconductor parameter analyzer and the results are shown in Fig. 8. The dark current levels are very low for this device when compared to similar QWIP designs. This is important for operating at high temperatures, where QWIPs typically suffer due to high dark current. The dark current showed an asymmetry similar to that of the responsivity, where the positive bias side shows significantly higher currents. In the dark current and photo current mechanisms, one common parameter is the gain, so an asymmetry in the gain is a likely source of this common asymmetry. We conjecture that this may be related to the inherent asymmetry of the physical structure of our QD-QW system, because the dot is placed to one side of the well. As illustrated in Fig. 9, depending on the bias an electron traveling in the continuum will have different capture probabilities since it will encounter a different sequence of potential profiles. In positive bias the electron first encounters low occupation probability area and will be less likely to be captured. We are currently performing quantitative analysis of this effect to verify and determine the extent of this effect.

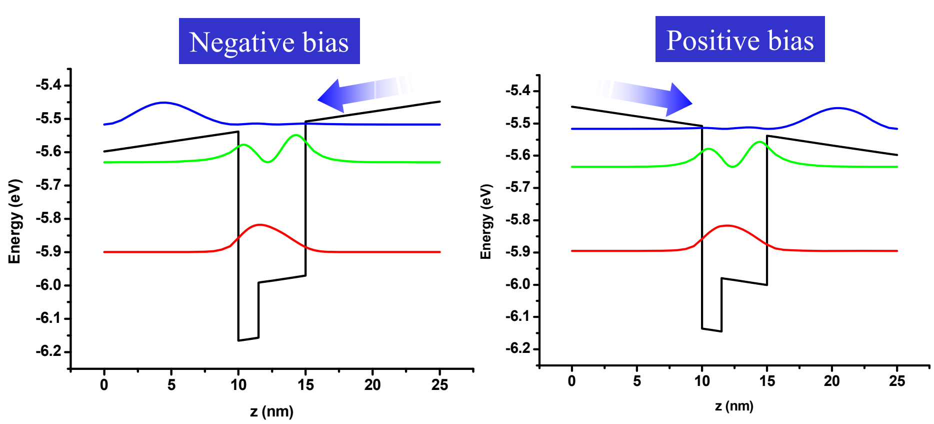

Fig. 9. Illustration of the wavefunctions and electron travel direction for our QDWIPs.

The noise current was measured using a Stanford Research Systems SR770 FFT spectrum analyzer. Noise current at temperatures below 150 K was not measurable because the noise level was below our system limit for the range of tested biases. From the dark current and noise current measurements, the dark current gain can be extracted according to the generation-recombination (GR) noise relation shown in Eq. 2., where i_{GR} is the GR noise, q is the fundamental charge, I_d is the dark current, g is the gain, and Δf is noise bandwidth.

$$i_{GR} = \sqrt{4qI_d g\Delta f} \Leftrightarrow g = \frac{i_{GR}{}^2}{4qI_d\Delta f} \tag{2}$$

The extraction of the gain can be tricky because one should take care to confirm that the measured noise and dark currents are in fact GR-limited. Any non-GR noise or leakage currents can cause a large error in the gain values. We believe that at high biases our devices do in fact have excess noise contributions because our gain modeling shows that we can reasonably expect gains of around 2 or 3 for our devices.[21] However, at high biases we extract gain values that are significantly higher than our model predicts. This prevents us from using this data to confirm the asymmetry in the gain that we conjectured on earlier in this paper.

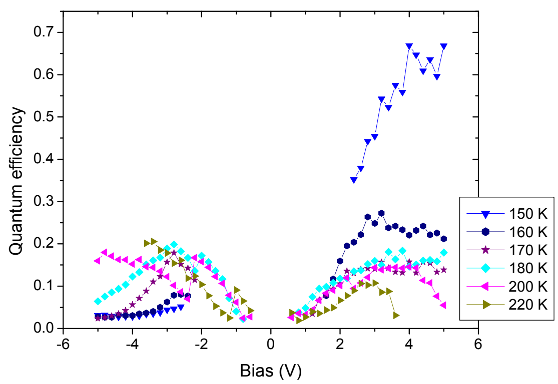

(a)

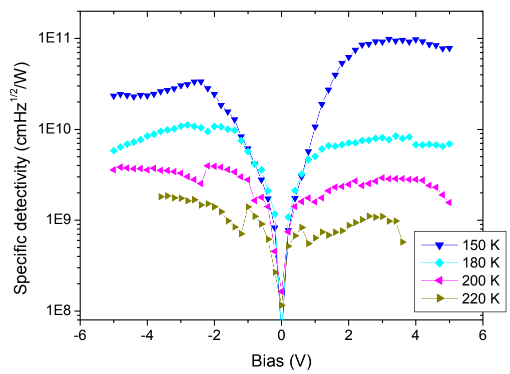

(b)

Fig. 10. (a) Internal quantum efficiency and (b) detectivity as a function of temperature and bias for our QDWIP

Fig. 10(a) shows the internal QE of the QDWIP. Assuming that the dark current and photo current gains are equivalent, the gain can be used to extract the internal quantum efficiency. The internal QE is extracted from the peak responsivity and gain via Eq. 3, where η_{int} is the internal quantum efficiency, R_p is the peak responsivity, h is Planck's constant, ν is the peak detection frequency, q is the fundamental charge, and g is the gain.

$$\eta_{\text{int}} = R_p \frac{h\nu}{q}\frac{1}{g} \tag{3}$$

This device shows an internal QE of 67% at 150 K and 5V. This is among the highest quantum efficiency values in the literature for a QD-based detector and an improvement over our previously demonstrated results.[20] Up to 220 K the internal QE is still as high as 20 %. The detectivity is shown in Fig. 10(b). At 150K operating temperature and biases >2V a D* of 1×10^{11} cmHz$^{1/2}$/W was achieved. The D* stayed in the 10^{10} cmHz$^{1/2}$/W range at temperatures up to 180K.

5. FOCAL PLANE ARRAY FABRICATION AND TESTING

For FPA testing, we fabricated our QDWIP device into an FPA. The FPA format was 320 × 256 with 30 μm pitch and 25 μm × 25 μm detectors. The pixel definition and metallization of the FPA were essentially the same as the test detector array fabrication, utilizing conventional UV photolithography, electron cyclotron resonance reactive ion etching, and metallization via electron beam metal evaporation and liftoff. After array fabrication, an Indigo

ISC9705 readout integrated circuit (ROIC) was hybridized to the FPA. The first step in this process was the creation of indium bumps on both the FPA and the ROIC dies. A thick photoresist layer with undercut profile suitable for lift-off processing of a thick indium layer was applied to the FPA die. After the photoresist patterning, an under bump metallization layer followed by a 6 μm thick indium layer were deposited via electron beam and thermal evaporation, respectively. Lift-off was performed by soaking in acetone. After a thorough sample cleaning process, the dies were flip chip bonded and underfilled with epoxy. Then, the FPA substrate was thinned using mechanical lapping and polishing. Finally, the hybridized die was mounted in and wire bonded to a leadless ceramic chip carrier.

The FPA was tested using a CamIRa FPA testing system from SE-IR Corp. The imaging system cryostat was equipped with a Ge window with 64 % transmission and a MWIR, f/2 ASIO series lens from Janos with 90 % transmission. All imaging and measurements were taken with a 300 K background.

In our previous work on FPAs using this class of InAs/InGaAs/InAlAs/InP QDWIP devices[22] the imaging was limited by the low responsivity levels at low bias and low temperature. A minimum temperature of ~120 K was required to achieve reasonable imaging. Our newer devices show improvement in both areas, however, the improvement at low temperature is the most apparent. The FPA performance was tested as a function of temperature up to 150 K. The FPA operating conditions were as follows: bias: -3 V, integration time: 30.41ms, frame rate: 32.64 Hz. Under these conditions, the ROIC capacitor did not approach saturation due to the dark current until the temperature was above 150 K. The imaging performance did not change greatly with temperature from 90 K to 120 K as indicated by the noise equivalent temperature difference (NEDT) plot in Fig. 11(a). A representative image taken at 120 K is shown in the inset of Fig. 11(a). The NEDT decreased slowly with temperature from 90 K to 120 K, due to the increasing responsivity with temperature. The noise was almost constant for this temperature range. Above 120 K, however, the performance began to decrease rapidly due to a decrease in responsivity above 110 K as shown in Fig. 11(b). This behavior is inconsistent with the large mesa experiments, which show the responsivity increasing with temperature up to around 150 K to 180 K. Also shown in Fig. 11(b) is the FPA dark current, which starts to increase quickly above 110 K. From the single device measurements, it can be seen that the optimal performance is still at biases greater than the ROIC can apply so reduction of the operating bias or a high operating bias ROIC is still necessary for optimal application of this detector to FPAs.

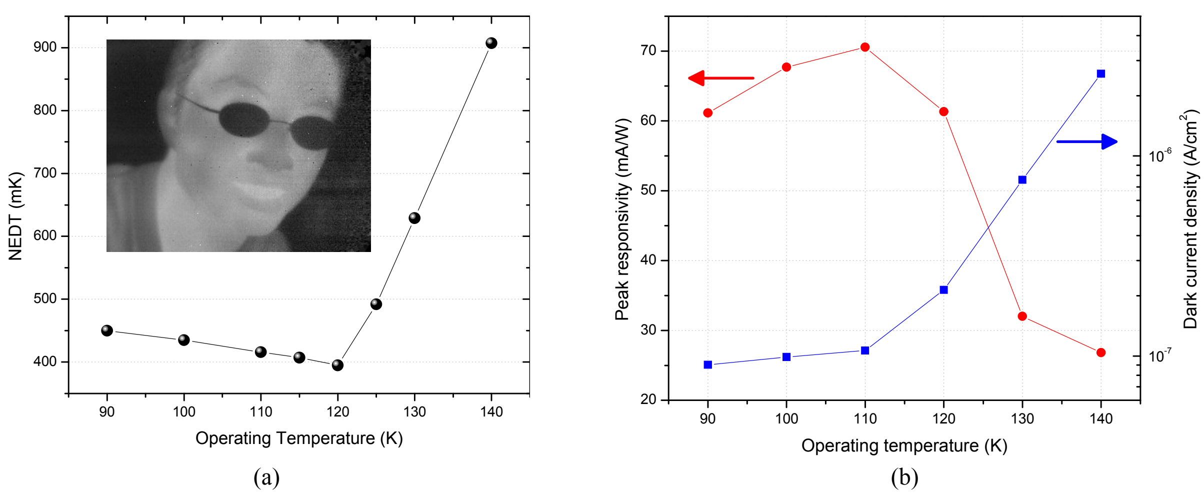

Fig. 11. (a) NEDT as a function of operating temperature with the inset showing a representative FPA image taken at an operating temperature of 120 K (b) the peak responsivity and dark current density of the FPA as a function of operating temperature.

6. CONCLUSION

In conclusion, we have developed a high-performance, high operating temperature InAs quantum-dot mid-infrared photodetector grown on InP substrate. The structure is unique compared to other QD-QW hybrid systems because of the very weak dot confinement. We have modeled the QD-QW system energy levels using finite element methods.

The peak detection wavelength of the device was observed at 3.9 µm, which comes from the QW transition. The peak responsivity and the specific detectivity at 150 K were 1.8 A/W and 1×10^{11} cmHz$^{1/2}$/W respectively. Low dark current density and an internal quantum efficiency of 67 % were obtained in this device. Focal plane array imaging based on this device structure was also demonstrated achieving an NEDT of ~400mK at 120 K.

REFERENCES

[1] V. A. Shchukin and D. Bimberg, "Spontaneous ordering of nanostructures on crystal surfaces," Rev. Mod. Phys. **71**, 1121 (1999).
[2] S. Chakrabarti, A. D. Stiff-Roberts, and P. Bhattacharya, "High-temperature operation of InAs-GaAs quantum-dot infrared photodetectors with large responsivity and detectivity," IEEE Photo. Technol. Lett. **16**, 1361 (2004).
[3] J. Szafraniec, S. Tsao, W. Zhang, H. Lim, M. Taguchi, A. A. Quivy, B. Movaghar, and M. Razeghi, "High-detectivity quantum-dot infrared photodetectors grown by metalorganic chemical-vapor deposition," Appl. Phys. Lett. **88**, 121102 (2006).
[4] E-T Kim, A Madhukar, Z Ye, and J. C. Campbell, "High detectivity InAs quantum dot infrared photodetectors," Appl. Phys. Lett. **84**, 3277 (2004).
[5] W Zhang, H Lim, M Taguchi, S Tsao, B Movaghar, and M Razeghi, "High-detectivity InAs quantum-dot infrared photodetectors grown on InP by metal-organic chemical-vapor deposition," Appl. Phys. Lett. **86**, 191103 (2005).
[6] J. Jiang, K. Mi, S. Tsao, W. Zhang, H. Lim, T. O'Sullivan, T. Sills, M. Razeghi, G. J. Brown, and M. Z. Tidrow, "Demonstration of a 256 x 256 middle-wavelength infrared focal plane array based on InGaAs/InGaP quantum dot infrared photodetectors," Appl. Phys. Lett. **84**, 2232 (2004).
[7] S Krishna, D Forman, S Annamalai, P Dowd, P Varangis, T Tumolillo, A Gray, J Zilko, K Sun, M Liu, J Campbell, and D Carothers, "Demonstration of a 320 x 256 two-color focal plane array using InAs/InGaAs quantum dots in well detectors," Appl. Phys. Lett. **86**, 193501 (2005).
[8] S-F Tang, C-D Chiang, P-K Weng, Y-T Gau, J-J Luo, S-T Yang, C-C Shih, S-Y Lin, and S-C Lee, "High-Temperature Operation Normal Incident 256 X 256 InAs-GaAs Quantum-Dot Infrared Photodetector Focal Plane Array," IEEE Photo. Technol. Lett. **18**, 986 (2006).
[9] S. D. Gunapala, S. V. Bandara, J. K. Liu, C. J. Hill, S. B. Rafol, J. M. Mumolo, J. T. Trinh, M. Z. Tidrow, and P. D. LeVan, "1024 × 1024 pixel mid-wavelength and long-wavelength infrared QWIP focal plane arrays for imaging applications," Semicond. Sci. Technol. **20**, 473 (2005).
[10] B. F. Levine, "Quantum-well infrared photodetectors," J. Appl. Phys. **74**, R1 (1993).
[11] V. Ryzhii, "The theory of quantum-dot infrared phototransistors," Semicond. Sci. Technol. **11**, 759 (1996).
[12] S. Chakrabarti, A. D. Stiff-Roberts, X. H. Su, P. Bhattacharya, G. Ariyawansa, and A. G. U Perera, "High-performance mid-infrared quantum dot infrared photodetectors," J. Phys. D: Appl. Phys. **38**, 2135 (2005).
[13] S. D. Gunapala, S. V. Bandara, Cory J. Hill, David Z. Ting, John. K. Liu, Sir B. Rafol, Edward R. Blazejewski, Jason M. Mumolo, Sam A. Keo, Sanjay Krishna, Y.-C. Chang, and Craig A. Shott, "640 x 512 pixels long-wavelength infrared (LWIR) quantum-dot infrared photodetector (QDIP) imaging focal plane array," IEEE J. Quant. Electron. **43**, 230 (2007).
[14] X Lu, J Vaillancourt, and M. J. Meisner, "Temperature-independent photoresponsivity and high-temperature (190 K) operation of a quantum dot infrared photodetector," Appl. Phys. Lett. **91**, 051115 (2007).
[15] E. Varley, M. Lenz, S. J. Lee, J. S. Brown, D. A. Ramirez, A. Stintz, S. Krishna, Axel Reisinger, and Mani Sundaram, "Single bump, two-color quantum dot camera," Appl. Phys. Lett. **91**, 081120 (2007).
[16] M. Califano and P. Harrison, "Presentation and experimental validation of a single-band, constant-potential model for self-assembled InAs/GaAs quantum dots," Phys. Rev. B **61**, 10959 (2000).
[17] S. Gangopadhyay and B. R. Nag, "Energy levels in three-dimensional quantum-confinement structures," Nanotechnology **8**, 14 (1997).
[18] E. Kane, "Band structure of indium antimonide," J. Phys. Chem. Solids **1**, 249 (1957).
[19] S. Tsao, H. Lim, H. Seo, W. Zhang, and M. Razeghi, "InP-Based Quantum-Dot Infrared Photodetectors With High Quantum Efficiency and High-Temperature Imaging," IEEE Sensors J. **8**, 936 (2008).
[20] H. Lim, S. Tsao, W. Zhang, and M. Razeghi, "High-performance InAs quantum-dot infrared photodetectors grown on InP substrate operating at room temperature," Appl. Phys. Lett. **90**, 131112 (2007).

[21] B. Movaghar, S. Tsao, S. Abdollahi Pour, T. Yamanaka, and M. Razeghi, "Gain and recombination dynamics in photodetectors made with quantum nanostructures: The quantum dot in a well and the quantum well," Phys. Rev. B **78**, 115320 (2008).
[22] S. Tsao, H. Lim, W. Zhang, and M. Razeghi, "High operating temperature 320 x 256 middle-wavelength infrared focal plane array imaging based on an InAs/InGaAs/InAlAs/InP quantum dot infrared photodetector," Appl. Phys. Lett. **90**, 201109 (2007).